

WATER, HIGH-ALTITUDE CONDENSATES, AND METHANE DEPLETION IN THE ATMOSPHERE OF THE WARM NEPTUNE WASP-107b

LAURA KREIDBERG^{1,2}

MICHAEL LINE³

CAROLINE MORLEY^{4,*}

KEVIN STEVENSON⁵

¹*Harvard Society of Fellows 78 Mt. Auburn St.*

Cambridge, MA 02138, USA

²*Harvard-Smithsonian Center for Astrophysics 60 Garden St.*

Cambridge, MA 02138

³*Arizona State University*

⁴*Harvard-Smithsonian Center for Astrophysics*

⁵*Space Telescope Science Institute*

Submitted to ApJL

ABSTRACT

We report a measurement of the near-infrared transmission spectrum of the warm Neptune exoplanet WASP-107b measured with the Hubble Space Telescope Wide Field Camera 3. We detect a water absorption feature (FIXME confidence). The feature is small amplitude, clouds. We combine an interior structure model of the planet with an atmospheric retrieval. We find an upper limit on the atmospheric metallicity of FIXME solar, a cloud deck.

Keywords: planets and satellites: individual (WASP-107b), planets and satellites: atmospheres

1. INTRODUCTION

2. OBSERVATIONS

We observed a single transit of WASP-107b with HST’s Wide Field Camera 3 (WFC3) instrument on UT 5-6 June 2017. The transit observation consisted of five HST orbits. At the beginning of each 96-minute orbit, we took an image of the target with the F130N filter (exposure time = 4.2 s). This direct image is used for wavelength calibration. For the remainder of the target visibility period (about 45 minutes), we obtained time series spectra with the G141 grism, which provides low-resolution spectroscopy over the wavelength range 1.1 – 1.7 μm . We used the NSAMP=6, SPARS_25 readout mode (exposure time = 112 s) to optimize the efficiency of the observations, as determined by the PandExo_HST planning tool¹. As is standard for observations of bright targets, we used the spatial scanning observing mode, which slews the telescope in the spatial direction over the course of an exposure. The scan rate was 0.12 arcseconds/sec.

3. DATA REDUCTION

We reduced the data with the custom pipeline described in Kreidberg et al. (2014), which we summarize briefly here. For each exposure, we extracted the spectrum from each up-the-ramp sample (or “stripe”) separately using the optimal extraction algorithm of Horne (1986). The stripe spectra were then summed to create the final spectrum. For each stripe, the extraction box was 80 pixels high and centered on the stripe’s midpoint in the spatial direction. To correct the change in dispersion solution over the length of the spatial scan, we interpolated each row to the wavelength scale of the row corresponding to the spectral trace. We also corrected for slight drift in the spectral direction (< 0.1 pixels) by interpolating each the first exposure. To subtract the background, we took the median of sky pixels that were uncontaminated by the target spectrum (rows 5 – 250, columns 5 – 15). The typical background counts were low: 40 photoelectrons/pixel, in comparison to 3×10^4 photoelectrons/pixel in the stellar spectrum.

4. ANALYSIS

The data analysis had two parts: the band-integrated “white” light curve fit and the spectroscopic light curve fits.

4.1. White Light Curve

To create the raw white light curve, we summed each spectrum over the 181 pixels in the spectral trace. The white light curve has systematic trends that are typical for WFC3 observations (Zhou et al. 2017): the flux increases asymptotically over each orbit (the “ramp” effect) and there is a visit-long linear trend. The largest ramp occurs in the initial orbit (orbit zero), so we only fit data from orbits one through four in our analysis, following common practice. We fit the light curve with the analytic model of the form $F_{\text{white}}(t) = S_{\text{white}}(t) \times T_{\text{white}}(t)$, where S_{white} is a systematics model and T_{white} is a transit model. We used the same systematics model as Kreidberg et al. (2015), Equation 1. To model the transit, we used the batman package (Kreidberg 2015). The transit model parameters are the orbital period p , time of inferior conjunction t_0 , transit depth r_p/r_s , ratio of semi-major axis to stellar radius a/r_s , orbital inclination i , and the quadratic stellar limb darkening parameters u_1 and u_2 .

4.1.1. Star Spot Crossing

In our initial analysis, we noticed a bump in the light curve during orbit three that was not fit well with our model. We attribute this feature to a star spot crossing event, as WASP-107 is an active star and spot crossings have been observed before (Dai & Winn 2017; Močnik et al. 2017). In our subsequent analysis, we gave the data in orbit three no weight in the fit. The amplitude of the spot crossing feature is 300 ppm, as illustrated in Figure 1.

4.1.2. Final Fit

In our final fit, we fixed the transit parameters a/r_s , i , p on the precise estimates from the Kepler light curve (Dai & Winn 2017). These values are consistent with our best fit when we allowed them to vary freely (and masked the star spot). We also fixed the limb darkening parameters on predictions from a PHOENIX model for a star with effective temperature 4300 K, calculated with the limb-darkening package from Espinoza & Jordán (2015). The remaining free parameters were t_0 , r_p/r_s , and the systematics parameters for the visit-long and orbit-long trends.

For the best fit white light curve, the root-mean-square (rms) residuals were 93 ppm (excluding the star spot crossing), which is somewhat larger than the expected shot noise of 50 ppm. We attribute the excess noise to loss of flux off the edge of the detector, which can occur if there is variation in the position or length of the spatial scan. There is no evidence for correlated noise in the residuals, so to account for the excess noise we simply increased the per-point uncertainties by a factor of 1.7 to achieve a reduced χ^2 value of unity. We then

¹ https://github.com/spacetelescope/PandExo_HST

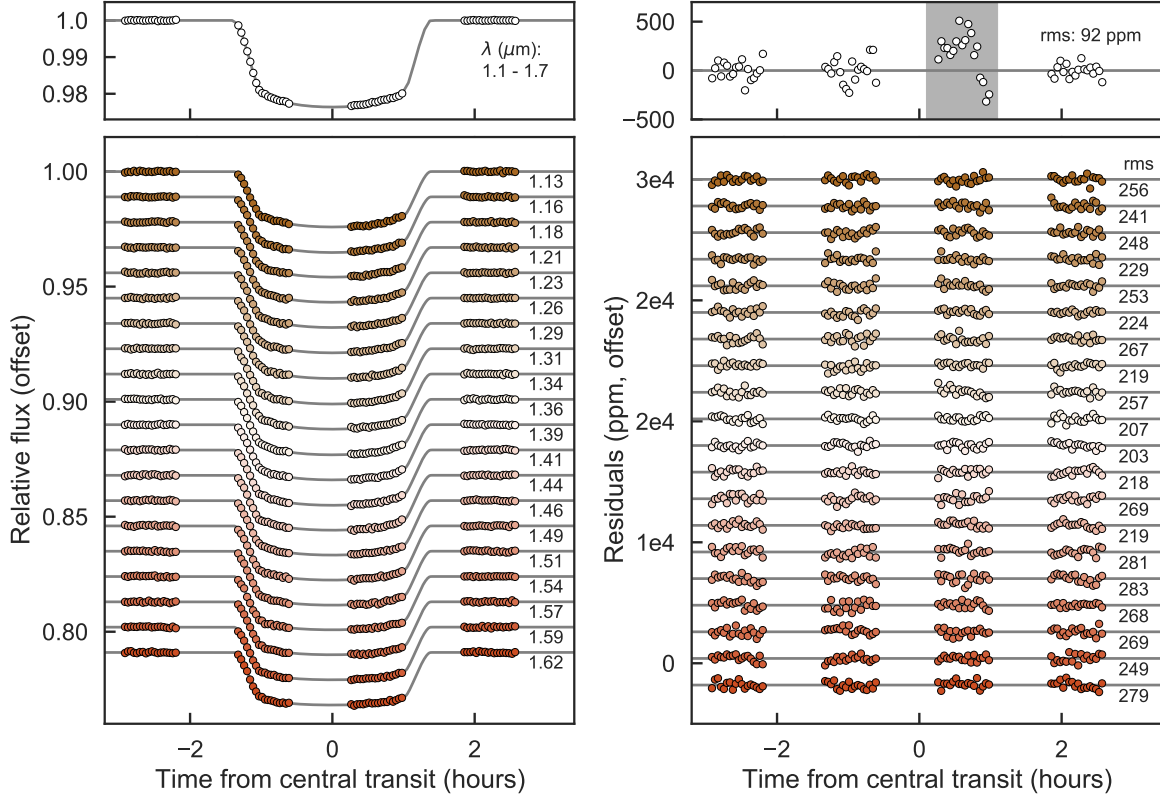


Figure 1. FIXME

used the Markov chain Monte Carlo (MCMC) algorithm to estimate parameter uncertainties (Foreman-Mackey et al. 2013). The chain had 50 walkers which each ran for 10^4 steps with the first 10% discarded as burn-in. We tested for convergence by dividing the chain in two halves and confirming that they gave consistent results. The transit time was $t_0 = 2457910.45407 \pm 6 \times 10^{-5}$ and the planet/star radius was $r_p/r_s = 0.14399 \pm 0.00017$.

4.2. Spectroscopic Light Curve Fits

We binned the spectrum into 20 spectrophotometric channels from 1.12 to 1.65 μm , shown in Figure 1. We fit the light curves with the `divide-white` technique, which assumes that the light curve systematics are nearly constant as a function of wavelength (Stevenson et al. 2014; Kreidberg et al. 2014). For this method, the transit model $T_\lambda(t)$ is multiplied by the systematics vector from the white light curve fit ($F_{\text{white}}/T_{\text{white}}$), and rescaled by a factor $C_\lambda + V_\lambda t$. An advantage of this approach is that it removes the star spot crossing feature, enabling us to use orbit three with no additional correction. There is a small chromatic effect due

to the changing amplitude of the spot crossing feature with wavelength, but this effect is not detectable in our data. As for the white light curve, we fixed some of the transit parameters on the estimates from Dai & Winn (2017) and fixed the limb darkening on the PHOENIX model. The fit had just three free parameters: C_λ , V_λ , and r_p/r_s .

The best fit light curves have a median reduced χ^2 value of 1.16. To ensure that we did not underestimate the uncertainty on the transit depths, we rescaled the photometric uncertainties for all spectroscopic channels such that the χ^2 values are unity. We performed an MCMC fit to the light curves with `emcee`. For each light curve we ran a fit with 50 walkers and 1000 steps per walker, and tested for convergence as we did for the white light curve. The median transit depths and 1σ uncertainties are given in Table 1.

We explored several alternative choices for the spectroscopic light curve fits, but found that none of them made a significant difference in the transmission spectrum. For example, we fit the spectroscopic light curves with the same analytic model we used for the white

light curve and obtained nearly identical relative transit depths (differing by just 0.3σ on average), except with a constant offset of 350 ppm. We attribute the offset to the uncorrected star-spot crossing feature. Regardless of the cause, the offset does not affect our final analysis, because the planet’s one-bar radius is a free parameter in the atmospheric retrieval (see §5). We also tried fitting for a linear limb darkening parameter rather than fixing the limb darkening on the PHOENIX model predictions, and found that the fitted limb darkening coefficients are consistent with the model. We opted to fix the coefficients in our final analysis because it improves the precision on the transit depths by about 10%. We also checked that the uncertainty in the stellar parameters does not significantly affect the PHOENIX model predictions at the level of precision of our data.

4.2.1. Transit Depths Redder than $1.62\ \mu\text{m}$

The red edge of the transmission spectrum is of interest for our analysis because methane is expected to be the dominant absorber over water at wavelengths greater than $1.6\ \mu\text{m}$. Unfortunately, we find that the our reddest spectroscopic light curves ($> 1.62\ \mu\text{m}$) are too poor in quality to robustly measure the transit depth. The residuals exhibit correlated noise and the fits have reduced $\chi^2_\nu > 2$. The transit depths are also sensitive to which method we use to fit for instrument systematics. We therefore opt not to report transit depths redder than the $1.62\ \mu\text{m}$ channel.

4.2.2. Independent Analysis

We also performed an independent data reduction and fit using K. Stevenson’s pipeline.

5. ATMOSPHERIC RETRIEVAL

We use the CHIMERA chemically-consistent transmission retrieval tool described in [Kreidberg et al. \(2015\)](#) to determine the basic atmospheric properties. Briefly, the transmission spectrum solves the transmission geometry problem using the equations in [Brown \(2001\)](#); [Tinetti et al. \(2012\)](#). We parametrize atmospheric composition with metallicity and carbon-to-oxygen ratio (C/O) under the assumption of thermochemical equilibrium using the NASA CEA routine (?) to compute the molecular abundances for H_2 , He, H_2O , CH_4 , CO, CO_2 , NH_3 , H_2S , Na, K, HCN, C_2H_2 , TiO, VO, and FeH. We have subsequently upgraded the transmission model to use correlated-K opacities ([Lacis & Oinas 1991](#); [Mollière et al. 2015](#); [Amundsen et al. 2016](#)) for the aforementioned gases generated from the pre-tabulated line-by-line cross section database ($dv/v\ 10^6$) described in [Freedman et al. \(2014\)](#). The transmission forward model is coupled with the powerful PyMultiNest

Table 1. WASP-107b transmission spectrum

Wavelength (μm)	Transit depth	Uncertainty
1.133	0.020641	5.9e-05
1.158	0.020733	5.5e-05
1.184	0.020505	5.6e-05
1.209	0.020498	5.4e-05
1.235	0.020455	5.9e-05
1.260	0.020492	5.0e-05
1.285	0.020620	6.2e-05
1.311	0.020739	5.0e-05
1.336	0.020660	5.7e-05
1.362	0.020858	4.8e-05
1.387	0.020794	4.8e-05
1.413	0.020888	5.2e-05
1.438	0.020821	6.2e-05
1.464	0.020691	5.1e-05
1.489	0.020682	6.9e-05
1.515	0.020679	6.7e-05
1.540	0.020509	6.0e-05
1.565	0.020480	6.4e-05
1.591	0.020500	5.6e-05
1.616	0.020514	6.5e-05

tool ([Buchner 2016](#)) to solve the parameter estimation and model selection problems.

The nominal model set-up requires a temperature-pressure profile (parameterized via the [Guillot 2010](#) relations), the atmospheric metallicity and carbon-to-oxygen ratio for molecular composition determination, disequilibrium properties crudely parameterized with nitrogen species and carbon species quench pressures ([Morley et al. 2017](#)), and aerosol properties. We experiment with three atmospheric scenarios within this setup (Table XX): Scenarios with and without methane, and with/without patchy cloud cover (as described and implemented in [Line et al. 2016](#). In all three scenarios we fix the T-P profile “shape” but scale the irradiation temperature, which incorporates unknown variables like the albedo and heat transport efficiency. T-P profile shape information is not readily retrievable, nor does it strongly influence information derived from WFC3 transmission spectra (e.g. [Kreidberg et al. 2015](#)). We also switch off the quench pressure param-

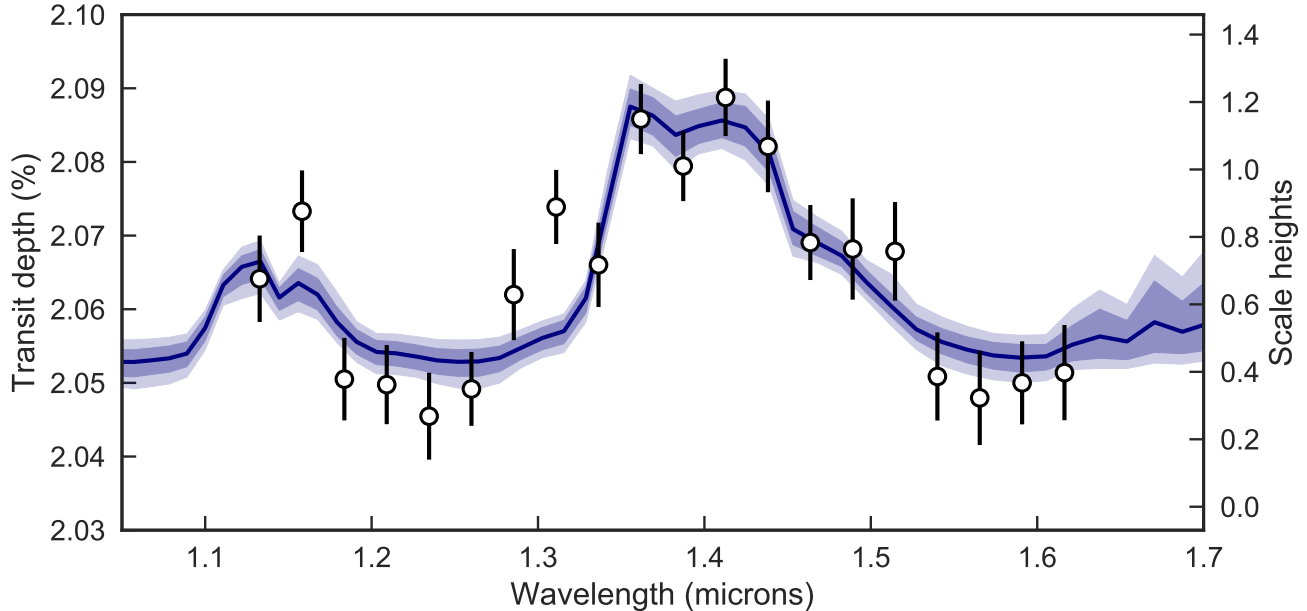


Figure 2. FIXME

ters as they are unlikely to strongly influence the equilibrium abundance profiles of the spectrally prominent, nearly constant-with-altitude abundance, species like CH_4 , H_2O , and NH_3 over this temperature range (e.g. Line et al. 2011; Moses et al. 2013). Aerosols are simply parameterized with a “gray cloud top pressure” with the option for cloud patchiness. We do not consider “sloped hazes” at this time as they are unlikely to influence the results.

6. DISCUSSION

We note that some directly imaged self-luminous planets in this temperature regime are also unexpectedly depleted in methane (e.g., Skemer et al. 2014), when compared to similar temperature brown dwarfs. The leading hypothesis of this depletion (?) is due to the CH_4 -CO quench point occurring in the CO stability field due to the low gravity of self-luminous planets when compared to brown dwarfs. In order this mechanism to work for neptune mass planet, the internal temperature would have to be near 500K to get the deep temperatures high enough to thermochemically deplete methane at the quench point. Given the age of the star, it is unlikely that such high internal temperatures are still due to heat of formation. It is possible that tidal heating could increase the internal temperature (Agundez et al. 2014; Morley et al. 2017) but that would require a negligible eccentricity, of which is currently uncertain for WASP107b.

6.1. Methane

6.2. Comparative planetology with HAT-P-11b, HAT-P-26b

6.3. Constraints on Condensate Properties

The amplitude of WASP-107b’s spectral features is about half that expected for an atmosphere free of condensates. In our retrieval analysis, we explored two simple parameterizations to model condensates: a gray opacity source and a sloped haze. The retrieved cloud-top pressure is FIXME at 1σ confidence.

We also considered physically motivated, self-consistent cloud and haze models based on . To model WASP-107b’s spectrum with self-consistent aerosols, we use the methods described in (Fortney et al. 2008; Morley et al. 2015). We include models from solar to $50\times$ solar metallicity and solar C/O ratio. We model clouds that form in cool atmospheres (Na_2S , KCl , ZnS , see Morley et al. 2012), varying the cloud sedimentation efficiency from 0.1 to 3. None of the cloudy models are sufficiently low amplitude to match the observed muted signal. We also model an ad hoc photochemical ‘soot’ layer near the top of the atmosphere, scaling results from previous photochemical models for GJ 436b (Line et al. 2011; Morley et al. 2017). With a sufficiently thick photochemical haze with particle sizes around 0.03 – 0.1 microns, the amplitude of the model water feature matches that of the observations.

6.4. Atmospheric Metallicity Predictions from Interior Structure Modeling

We determine the bulk metallicity of WASP-107 b using the structure evolution modeling of Thorngren et al. (2016). These consider a thermally inert heavy-element core with a convective envelope of additively mixed H/He (Saumon et al. 1995) and heavy-element impurities. The heavy-elements were a 50-50 rock-ice mix from ANEOS (Thompson 1990). Planets were evolved in time using the atmospheric models of Fortney (2007). We explored possible envelope metallicities and core masses using a metropolis-hastings MCMC with $M = .12 \pm .03$, $R = .94 \pm .02$, and the age as alternatively .2-1.0 Gyr or 1.0-13.8 Gyr. Priors were $\propto 1$ in envelope metal mass fraction and core mass. The MCMC burned in for 1000 steps and then collected 4,000,000 samples, thinned down to 100,000. The resulting envelope metal mass fractions were converted to metallicities by assum-

ing the mean molecular weight of the metals was about 18 (the value for water), using the approach of Fortney (2013).

7. FUTURE PLANS

WASP-107b is slated to be observed with numerous facilities. Transits were recently observed with the WFC3/G102 grism and Spitzer 3.6 and 4.5 μm channels. Spitzer eclipses are planned (Program FIXME; PI L. Kreidberg). In addition, WASP-107b is included in the *JWST* Guaranteed Time Observations.

Combine data from Spitzer/HST JWST GTO

Fei Dai Jessica Spake

L.R.K. acknowledges support from the Harvard Society of Fellows and the Harvard Astronomy Department Institute for Theory and Computation.

Facilities: HST(WFC3)

REFERENCES

- Amundsen, D. S., Mayne, N. J., Baraffe, I., et al. 2016, *A&A*, 595, A36
- Brown, T. M. 2001, *ApJ*, 553, 1006
- Buchner, J. 2016, PyMultiNest: Python interface for MultiNest, Astrophysics Source Code Library, , , ascl:1606.005
- Dai, F., & Winn, J. N. 2017, *AJ*, 153, 205
- Espinoza, N., & Jordán, A. 2015, *MNRAS*, 450, 1879
- Foreman-Mackey, D., Hogg, D. W., Lang, D., & Goodman, J. 2013, *PASP*, 125, 306
- Fortney, J. J., Lodders, K., Marley, M. S., & Freedman, R. S. 2008, *ApJ*, 678, 1419
- Freedman, R. S., Lustig-Yaeger, J., Fortney, J. J., et al. 2014, *ApJS*, 214, 25
- Guillot, T. 2010, *A&A*, 520, A27
- Horne, K. 1986, *PASP*, 98, 609
- Kreidberg, L. 2015, *PASP*, 127, 1161
- Kreidberg, L., Bean, J. L., Désert, J.-M., et al. 2014, *Nature*, 505, 69
- Kreidberg, L., Line, M. R., Bean, J. L., et al. 2015, *ApJ*, 814, 66
- Lacis, A. A., & Oinas, V. 1991, *J. Geophys. Res.*, 96, 9027
- Line, M. R., Vasisht, G., Chen, P., Angerhausen, D., & Yung, Y. L. 2011, *ApJ*, 738, 32
- Line, M. R., Stevenson, K. B., Bean, J., et al. 2016, *AJ*, 152, 203
- Mollière, P., van Boekel, R., Dullemond, C., Henning, T., & Mordasini, C. 2015, *ApJ*, 813, 47
- Morley, C. V., Fortney, J. J., Marley, M. S., et al. 2012, *ApJ*, 756, 172
- . 2015, *ApJ*, 815, 110
- Morley, C. V., Knutson, H., Line, M., et al. 2017, *AJ*, 153, 86
- Moses, J. I., Madhusudhan, N., Visscher, C., & Freedman, R. S. 2013, *ApJ*, 763, 25
- Močnik, T., Hellier, C., Anderson, D. R., Clark, B. J. M., & Southworth, J. 2017, *MNRAS*, 469, 1622
- Stevenson, K. B., Bean, J. L., Seifahrt, A., et al. 2014, *AJ*, 147, 161
- Tinetti, G., Tennyson, J., Griffith, C. A., & Waldmann, I. 2012, *Philosophical Transactions of the Royal Society of London Series A*, 370, 2749
- Zhou, Y., Apai, D., Lew, B. W. P., & Schneider, G. 2017, *AJ*, 153, 243